Rotationally resolved spectroscopy of the $\tilde{A}\,^2A_1 \leftarrow \tilde{X}\,^2B_1$ transition of H_2S^+ above the barrier to linearity using the mass-analyzed threshold ionization photofragment excitation technique

Songhee Han, Tae Yeon Kang,[a] and Sang Kyu Kim[b]
Department of Chemistry and KI for Nanocentury, KAIST, Daejeon (305-701), Republic of Korea

(Received 30 October 2009; accepted 9 February 2010; published online 26 March 2010)

The $\tilde{A}\,^2A_1 \leftarrow \tilde{X}\,^2B_1$ transitions of H_2S^+ above the barrier to linearity have been investigated with the energy resolution high enough to identify individual rotational transition lines for the first time. The rotational cooling of the cation is achieved either by the direct ionization or mass-analyzed threshold ionization (MATI) technique employed in the vacuum-ultraviolet laser excitation of the jet-cooled H_2S. Subsequent photoexcitation leads to the $H_2S^+ \rightarrow H_2 + S^+$ dissociation and the S^+ product yield taken as a function of the excitation energy gives the photofragment excitation (PHOFEX) spectra. The combined use of MATI and PHOFEX techniques greatly simplifies the spectrum allowing the accurate identification of the rotationally resolved bands which is otherwise a formidable task due to the intrinsic complexity of the $\tilde{A}\,^2A_1 \leftarrow \tilde{X}\,^2B_1$ transition. Highly excited states of $\tilde{A}(0,7,0)$, $\tilde{A}(0,8,0)$, and $\tilde{A}(0,9,0)$ vibronic levels with different K quantum numbers which are located above the barrier to linearity are thoroughly investigated. The bent-to-quasilinear transition of H_2S^+ above the barrier to linearity shows the characteristics of the Renner–Teller effect, showing the large A rotational constant and strong intensity borrowing of the highly vibrationally excited ground levels such as $\tilde{X}(0,23,0)$ or $\tilde{X}(0,24,0)$ in the dipole-allowed excitation. Spectroscopic parameters of term values, rotational, and spin-orbit coupling constants are precisely determined in this work, providing the most quantitative spectroscopic structure of the H_2S^+ to date. Quantum-state dependent photodissociation dynamics are also discussed from spectral features of PHOFEX. © *2010 American Institute of Physics*. [doi:10.1063/1.3358252]

I. INTRODUCTION

Hydrogensulfide cation (H_2S^+) has been intensively studied for the investigation of the nonadiabatic Renner–Teller coupling effect on molecular structure and dynamics as a prototypical model system.[1–8] Although energy minimum structures in both $\tilde{A}\,^2A_1$ and $\tilde{X}\,^2B_1$ electronic states of H_2S^+ adopt the bent geometry it is well known that two electronic states are correlated with a single degenerate electronic state ($^2\Pi_u$) at the linear configuration to form the Renner–Teller pair.[9] The drastic change in the equilibrium bent angle between ground ($\tilde{X}\,^2B_1$) and first excited states ($\tilde{A}\,^2A_1$) of H_2S^+ induces the strong Renner–Teller coupling accompanying with the large fluctuating spin-orbit coupling, leading to the complex spectroscopic structures especially above the barrier to linearity. Among many theoretical and experimental studies,[10–19] for instance, Baltzer and co-workers[2,20] had reported the He (I) photoelectron spectrum of H_2S to identify various $\tilde{A}\,^2A_1$ vibronic states of H_2S^+ as well as highly excited $\tilde{X}\,^2B_1$ levels based on the model Hamiltonian suggested by Duxbury and colleagues which includes Renner–Teller and spin-orbit couplings. More recently Ng and colleagues reported the photoelectron spectrum with the improved spectral resolution using the pulsed-field ionization technique combined with the synchrotron radiation source, giving the quantitatively refined data for the value of barrier to linearity rotational constants, and vibronic term values associated with the photoionization processes producing H_2S^+ in various electronic states of $\tilde{X}\,^2B_1$, $\tilde{A}\,^2A_1$ or $\tilde{B}\,^2B_2$.[21] Despite these two detailed spectroscopic studies in addition to many other previous works, the quantum states of H_2S^+ have not been rotationally resolved yet, hampering the precise determination of the spectroscopic structure of H_2S^+, especially in the energy region near or above the barrier to linearity.

In this work, the H_2S sample was supersonically cooled and the vacuum-ultraviolet (VUV) laser pulse with the bandwidth of ~ 1 cm^{-1} was used for the ionization. In the ionization process, we have employed the direct ionization or mass-analyzed threshold ionization (MATI) technique[22,23] in order to rotationally cool down or select just a few rotational levels of the ground state H_2S^+ ($\tilde{X}\,^2B_1$), respectively. The subsequent photoexcitation corresponding to the $\tilde{A}\,^2A_1 \leftarrow \tilde{X}\,^2B_1$ transition of H_2S^+ induces the dissociation into $H_2 + S^+$ products. Through monitoring the S^+ yield as a function of the photoexcitation energy, the photofragment excitation (PHOFEX) spectrum has been obtained to give the highly resolved rotational bands with signal intensities reflecting

[a]Present address: Korea Institute of Science and Technology, Seoul (136-791), Republic of Korea.
[b]Author to whom correspondence should be addressed; Electronic mail: sangkyukim@kaist.ac.kr.

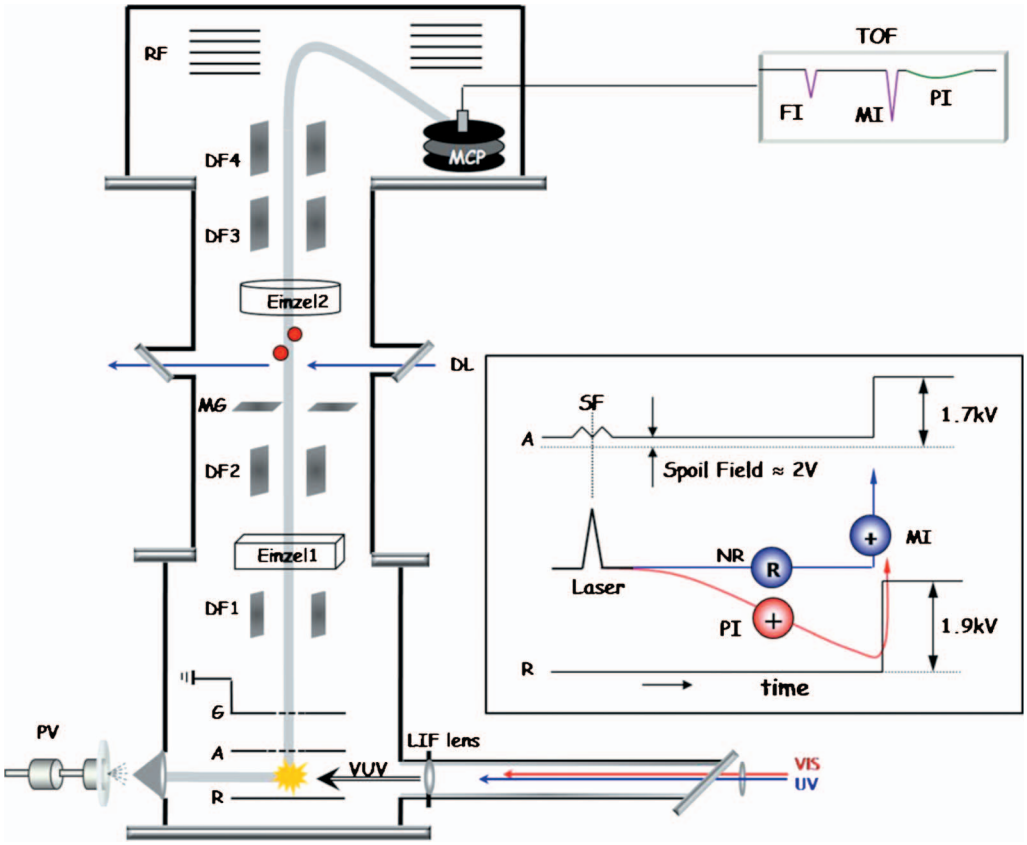

FIG. 1. Experimental setup used for PHOFEX and MATI-PHOFEX spectra. A: accelerator plate, DF: deflector plates, DL: dissociation UV laser, FI: fragment ion, G: ground, MCP: microchannel plates, MG: mass gate, MI: MATI ion, NR: neutral Rydberg, PV: pulsed valve, PI: prompt ion, R: repeller plates, RF: reflectron, SF: scrambling field. Ion guide is shown with gray broad lines. The inset is the electric field scheme for the generation of MATI ions (see the text in Sec. II).

both $\tilde{A}\ ^2A_1 \leftarrow \tilde{X}\ ^2B_1$ transition oscillator strengths and associated fragmentation efficiencies. MATI-PHOFEX technique[24,25] employed in this work turns out to be extremely useful to identify the rotational transitions not only in terms of the improvement of the energy resolution but also the strict symmetry selection rules in the dipole-allowed transition. We have also found new spectral features in the optical excitation spectrum of H_2S^+, revealing the complicated nature of the nonadiabatic Renner–Teller interaction.

II. EXPERIMENT

Hydrogen sulfide was purchased from Aldrich (99.5 +%) and used without further purification. The sample was diluted to the 10% mixture by addition of the Ar gas and expanded into vacuum through a 0.8 mm diameter nozzle orifice (General Valve Series 9) with a backing pressure of ~2 atm. The supersonic jet was collimated through a 1 mm diameter skimmer (Precision) prior to be collinearly overlapped with the VUV laser pulse which was generated via the four-wave mixing in a Kr gas cell using the UV laser pulse fixed at 202.316 nm for the Kr $4s^24p^5(^2P^\circ_{1/2})5p[1/2]_0 - 4s^24p^6$ transition and the tunable visible laser pulse for the VUV wavelength scanning. The dye laser output (Lambda phisik, Scanmate 2) pumped by the third harmonic of a Nd:yttrium aluminum garnet (YAG) laser (Continuum, Precision 2) was frequency doubled through a KD*P (HT-20/310, tuning range 300–380) crystal, rotated by 90° in the linear polarization axis through a $\lambda/2$ waveplate, and mixed with the fundamental on a Barium Borate (BBO) crystal to generate the UV laser pulse at 202.316 nm. Another dye laser (Lumonics, HD-500) output in 689–697 nm range was generated by the same Nd:YAG laser. The resultant VUV laser pulse was spatially separated from the UV and VIS fundamentals using the edge of the collimating LiF lens placed on the exit of the Kr cell in which the pressure was maintained at ~1 Torr, and collinearly overlapped with the molecular beam in a counter propagating manner, Fig. 1. The pulsed field of 140–220 V/cm was applied to ionize the long-lived Rydberg manifolds prepared by VUV excitation (λ=118.38–118.68 nm) with a delay time of ~8 μs after the laser irradiation. The discriminating spoil field of ~2 V/cm was used to separate out the directly formed ions. In obtaining MATI spectrum of Fig. 2(a), the pulsed field of ~5 V/cm was used for reducing the linewidth of the spectral bands while other conditions were same as above. For PHOFEX or MATI-PHOFEX spectra, the third dye laser output (Continuum, ND6000) in the 387–425 nm range with $\Delta\bar{\nu}$=0.5 cm^{-1} was used to excite H_2S^+ ions. As shown in Fig. 1, $H_2\ ^{32}S^+$ ions generated by direction ionization or MATI technique were repelled and accelerated along the time-of-flight axis. After a couple of deflecting and focusing ion optics, the ion species corresponding to the mass of $H_2\ ^{32}S^+$ was exclusively chosen by applying the optimally delayed pulsed field at the mass gate.

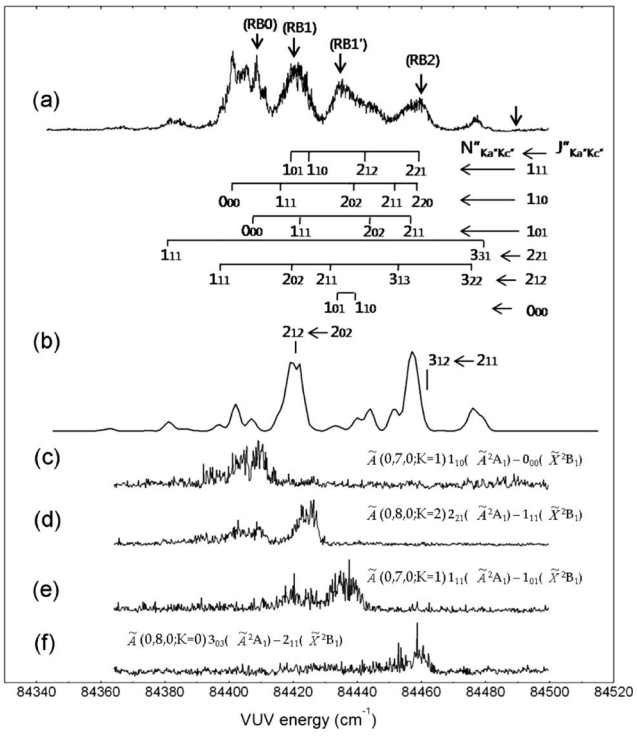

FIG. 2. (a) VUV one-photon MATI spectrum of H_2S^+ is shown with (b) the simulation at the rotational temperature of 30 K where the intensity ratio of the *C*-type and *A*-type transitions is set to 3:1. The arrows indicate in upper trace represent RB0, RB1, RB1′, and RB2 bands (from left to right) used to select rotational states of H_2S^+ in the ground state for the MATI-PHOFEX spectra. For the PHOFEX spectrum, the VUV energy indicated by an arrow in the high energy region was used for ionization. The S^+ yield spectra, (c)–(f) are obtained by monitoring the S^+ fragment yield as a function of VUV energy at fixed rovibronic transitions of H_2S^+ as denoted above each spectrum (see the text).

The photodissociation laser pulse was given to the ion cloud on the flight to induce the chemical bond dissociation into $H_2+{}^{32}S^+$ products. The $^{32}S^+$ product was separated in the time domain from the parent by the reflectron ion optics before being detected in the microchannel plates. For the verification of the long-lived Rydberg states of H_2S, the photoionization laser wavelength was fixed at a specific rovibronic transition where the VUV laser wavelength was scanned in the MATI experimental condition. The ion current was digitized by an oscilloscope (LeCroy, LT584M) and stored in a personal computer which was also used to control dye lasers. The wavelengths of dye laser outputs were calibrated using a wavemeter (Coherent; Wavemaster) with the accuracy of ± 0.5 cm^{-1}.

III. RESULTS AND DISCUSSION

A. MATI spectrum of $H_2S^+(\tilde{X}\,^2B_1) \leftarrow H_2S(\tilde{X}\,^1A_1)$

The MATI spectrum shows rotationally-resolved transitions involved in the direct VUV photoionization from $H_2S(\tilde{X}\,^1A_1)$ to $H_2S^+(\tilde{X}\,^2B_1)$ near the adiabatic ionization threshold region, Fig. 2. The rotational transitions from $J''_{Ka''Kc''}$ to $N''_{Ka''Kc''}$ (H_2S^+) are appropriately assigned based on the asymmetric rotor simulation at $T_{rot}=30$ K. It is found however that the MATI spectrum is not so well reproduced by the asymmetric rotor simulation, suggesting that Rydberg manifolds converging to each rotational state of the cation may be severely perturbed in the MATI excitation scheme possibly because of extraordinary long lifetimes of autoion-

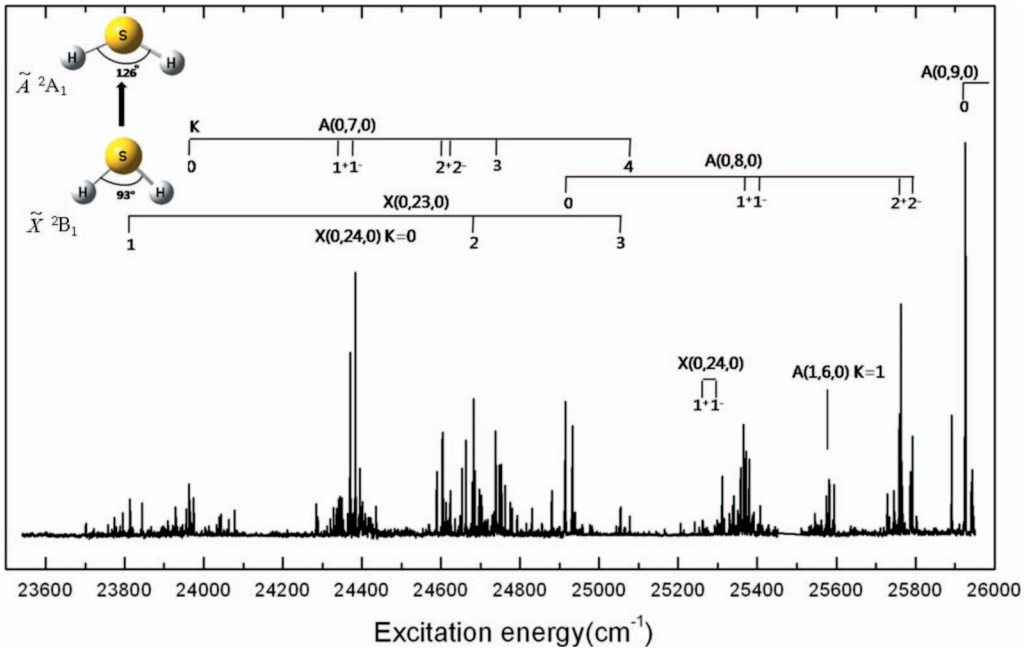

FIG. 3. The PHOFEX spectrum of H_2S^+ with assignments according to vibronic term values in Table I. Notations are described in the text. Superscripts of +/− represent (+1/2)/(−1/2) spin-orbit components, respectively.

TABLE I. Vibronic term values of H_2S^+ with different K quantum numbers.

	PFI-PES[a]		He(I)-PES[b]		Calculation[c]
PHOFEX (this work)	Assignment	Energy (cm^{-1})	Assignment	Energy (cm^{-1})	Energy (cm^{-1})
	$\tilde{X}(0,23,0;K=0)$	23 622	$\tilde{X}(0,22,0;K=2)$	23 617	23 498
	$\tilde{A}(0,6,0;K=4)$	23 685	$\tilde{A}(0,5,0;K=3)$	23 741	23 829
23 813[d]	$\tilde{X}(0,23,0;K=1)$	23 825	$\tilde{A}(0,6,0;K=0)$	23 941	24 030
23 963[d]	$\tilde{A}(0,7,0;K=0)$	23 952	$\tilde{X}(0,23,0;K=1)$	24 029	24 079
		23 944[e]	$\tilde{X}(0,22,0;K=3)$		24 143
			$\tilde{X}(0,22,0;K=4)$	24 140	24 176
24 341[f] 24 378[g]	$\tilde{A}(0,7,0;K=1)$	24 331 24 337[e]	$\tilde{A}(0,6,0;K=1)$	24 343	24 434
24 383[h]	$\tilde{A}(0,24,0;K=0)$				
24 604[i] 24 624[j]	$\tilde{A}(0,7,0;K=2)$	24 522	$\tilde{A}(0,6,0;K=2)$		24 474
24 683[d]	$\tilde{X}(0,23,0;K=2)$	24 631	$\tilde{X}(0,23,0;K=2)$	24 643	24 805
24 738[d]	$\tilde{A}(0,7,0;K=3)$	24 774	$\tilde{A}(0,6,0;K=3)$	24 748	24 853
24 915[h]	$\tilde{A}(0,8,0;K=0)$	24 916	$\tilde{A}(0,7,0;K=0)$	24 903	24 974
25 054[d]	$\tilde{X}(0,23,0;K=3)$	25 041	$\tilde{X}(0,23,0;K=3)$	24 966	25 168
25 077[d]	$\tilde{A}(0,7,0;K=4)$	25 120	$\tilde{A}(0,6,0;K=4)$	25 099	25 240
25 261[f] 25 298[g]	$\tilde{X}(0,24,0;K=1)$				
25 367[f] 25 407[g]	$\tilde{A}(0,8,0;K=1)$	25 342	$\tilde{A}(0,7,0;K=1)$ $\tilde{X}(0,23,0;K=4)$	25 339	25 418 25 539
25 582[d]	$\tilde{A}(1,6,0;K=1)$	25 579	$\tilde{A}(1,5,0;K=1)$	25 686	
25 763[i] 25 792[j]	$\tilde{A}(0,8,0;K=2)$	25 751	$\tilde{A}(0,7,0;K=2)$	25 773	25 929
25 926[h]	$\tilde{A}(0,9,0;K=0)$	25 909	$\tilde{A}(0,8,0;K=0)$	25 906 25 991	25 974 26 224

[a]Obtained by the subtraction of IE (10.4689 eV) from vibronic energies in Ref. 21.
[b]Obtained by the subtraction of IE (10.4666 eV) from vibronic energies in Ref. 20.
[c]Obtained by the subtraction of IE (10.4666 eV) from calculated vibronic energies in Refs. 2 and 20.
[d]Maximum peak positions in PHOFEX spectra.
[e]Vibronic origins obtained from the spectra in Ref. 21.
[f]Term value for the branch ${}^RR_{0,0}$ of (+)1/2 component of $K=1$ vibronic bands.
[g]Term value for the branch ${}^RR_{0,0}$ of (−)1/2 component of $K=1$ vibronic bands.
[h]Term value for the branch ${}^PQ_{1,1}$ of $K=0$ vibronic bands.
[i]Term value for the branch ${}^RR_{1,1}$ of (+)1/2 component of $K=2$ vibronic bands.
[j]Term value for the branch ${}^RR_{1,1}$ of (−)1/2 component of $K=2$ vibronic bands.

izing states above the adiabatic ionization energy (IE). Consequently, individual rotational transitions are apparently broad and the relative intensities do not correctly reflect the Boltzmann temperature with respect to the rotational degrees of freedom. It is interesting to note that the previously reported zero-electron kinetic energy (ZEKE) spectrum[26] had been well reproduced by the asymmetric rotor simulation and this should be due to the much smaller electric field used in the ZEKE ionization compared to the PFI field of 5 V/cm employed in the MATI excitation scheme. Nonetheless, the selection of the specific rotational transition in the MATI spectrum makes possible the population of $H_2S^+(\tilde{X}\,{}^2B_1)$ to be concentrated in a few rotational quantum states. The arrows in Fig. 2 are the rotational transitions used to select the initial rotational levels of H_2S^+ for corresponding MATI-PHOFEX spectra. For instance, by the ionization through the rotational band at 84 408 cm^{-1} (RB0), the $0_{00}(N''_{Ka''Kc''})$ state of H_2S^+ in the $\tilde{X}\,{}^2B_1$ state should be mainly populated. It should be noted that the nuclear spin is conserved in the ionization process. Namely, the 0_{00} state of the cation is generated from $1_{10}(J''_{Ka''Kc''})$ or 1_{01} state of H_2S in the ground state as the rotational state with K_a+K_c=odd (even) is ortho (para) in the neutral ground $H_2S(\tilde{X}\,{}^1A_1)$ while $H_2S^+(\tilde{X}\,{}^2B_1)$ is ortho (para) when K_a+K_c is even (odd). Similarly, the $1_{11}(\tilde{X}\,{}^2B_1)$ state (ortho) is most populated by the RB1 transition at 84 420 cm^{-1} whereas the small contribution of the 1_{01} state (para) is also expected. The 1_{01} state becomes the major population when the RB1′ transition at 84 434 cm^{-1} is used in the MATI scheme whereas the 2_{11} state (ortho) can be mainly populated using the RB2 transition at 84 460 cm^{-1}, Fig. 2. In our MATI spectrum, the adiabatic IE corresponding to the nuclear-spin forbidden $0_{00}-0_{00}(N''_{Ka''Kc''}-J''_{Ka''Kc''})$ transition is estimated to be $84\,421\pm10$ cm^{-1}, which is slightly lower than but consistent within uncertainties with the previously reported value of $84\,432\pm2$ cm^{-1} from ZEKE studies. The discrepancy may originate from the mutual interaction of long-lived Rydberg manifolds converging to different cationic states which seems to be quite significant in the MATI excitation scheme *(vide supra)*. For the PHOFEX spectrum, the VUV IE has been fixed at 84 489 cm^{-1} to generate all rotational states of H_2S^+ populated by the ionization of the jet-cooled H_2S

B. PHOFEX of $H_2S^+(\tilde{A}\,{}^2A_1 \leftarrow \tilde{X}\,{}^2B_1)$

The PHOFEX spectrum taken by monitoring the S^+ yield as a function of the photoexcitation laser wavelength is

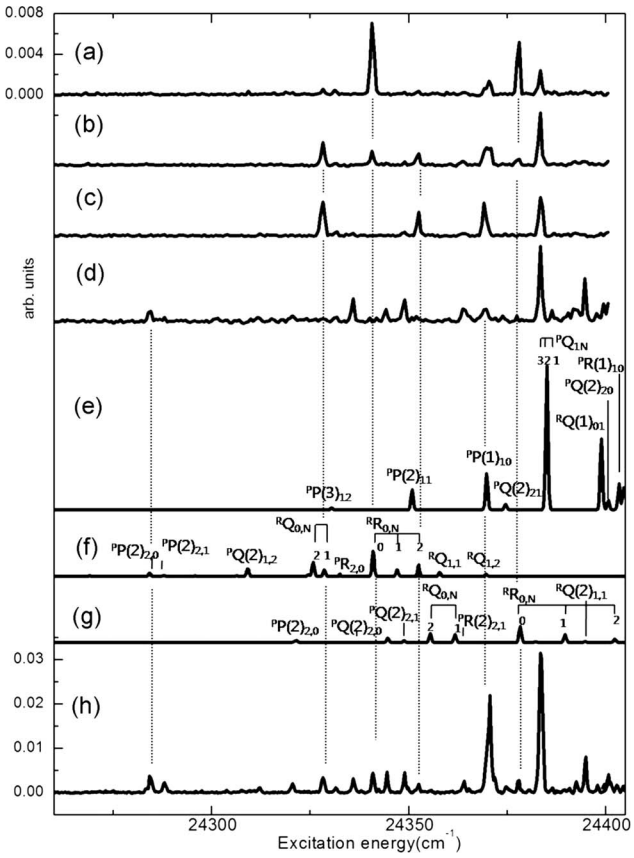

FIG. 4. MATI-PHOFX and PHOFEX spectra of $\tilde{A}(0,7,0;K=1)$ and $\tilde{X}(0,24,0;K=0)$ bands. (a)–(d) represent MATI-PHOFEX spectra taken via RB0, RB1, RB1′, and RB2 transitions, respectively. All bands are denoted by $^{\Delta Ka}\Delta N_{Ka'',Kc''}$ whereas N'' values are shown in parentheses for the clarity. The simulations for (e) $\tilde{X}(0,24,0;K=0)$, (f) $\tilde{A}(0,7,0;K=1)^+$, and (g) $\tilde{A}(0,7,0;K=1)^-$ are presented, in which (f) and (g) represent (+)1/2 and (−)1/2 spin-orbit states, respectively. Detailed values involved in the rovibronic transitions are listed in Tables II and III. The (h) PHOFEX spectrum shows the overall pattern of the various transitions in the same energy region at the rotational temperature at 30K.

shown in Fig. 3. The VUV laser excitation fixed at 84 489 cm^{-1} generates the $H_2S^+(\tilde{X}\ ^2B_1)$ ion populated over several rotational states according to the Boltzmann distribution at $T_{rot}=30$ K. Since the S^+ yield is monitored in the PHOFEX spectrum, the photoexcitation energy should be higher than the reaction thresholds for the H_2+S^+ dissociation channel. Actually, the PHOFEX signal starts to appear at ~23 700 cm^{-1}, corresponding to the reaction threshold energy for the $H_2S^+ \rightarrow H_2+S^+$ dissociation channel. It should be noted that even though the VUV laser energy used in the PHOFEX is ~51 cm^{-1} higher than the adiabatic IE, the appearance energy of the S^+ product starting from neutral ground H_2S is the sum of IE and the threshold energy given by the photoexcitation laser frequency because of the energy loss via the kinetic energies of photoelectrons in the VUV ionization process. Consequently, the appearance energy of S^+ is estimated to be ~13.406 eV (108 120 cm^{-1}), and this is ~200 cm^{-1} lower than the previously value of 13.43 eV reported by the Eland group,[27] determined from the photoelectron-photoion coincidence spectroscopy. The PHOFEX spectrum gives rotationally resolved bands with a spectral linewidth of ~0.7 cm^{-1}. The H_2S^+ dissociation reaction has been much studied.[28–34] Accordingly, the excited $\tilde{A}$ state of H_2S^+ internally converts to the highly excited $\tilde{X}$ state via the efficient Renner-Teller coupling, and this is followed by the spin-orbit coupling to the repulsive quartet state. The Renner–Teller coupling is significant at the linear configuration whereas the coupling to the dissociation continuum occurs at the strongly bent geometry, suggesting that two cooperative processes interestingly occur at two distinctly different nuclear configurations. This is consistent with the experimental fact that the each band is quite narrow and symmetric, implying that the excited vibronic $\tilde{A}\ ^2A_1$ state is not subject to direct coupling to the dissociation continuum. Although the detailed and accurate spectral assignments for individual rovibronic transitions turn out to be plausible only when MATI-PHOFEX spectra taken via various initial rotational transitions are analyzed (*vide infra*), the overall vibronic assignment seems to be quite helpful in understanding the structural and dynamical features of H_2S^+ above the barrier to linearity.

Since H_2S^+ in the $\tilde{A}\ ^2A_1$ state has a minimum energy at the HSH bent angle of 126° whereas the $\tilde{X}\ ^2B_1$ state adopts the bent angle of 93°,[1] the highly vibrationally excited states in the ν_2 bending mode are activated in the $\tilde{A}\ ^2A_1-\tilde{X}\ ^2B_1$ transition. It should be noted that $\tilde{A}\ ^2A_1$ and $\tilde{X}\ ^2B_1$ states of H_2S^+ become degenerate at the linear geometry, giving rise to the strong Renner–Teller interaction. The barrier to linearity had been estimated to be 23 209 cm^{-1} for $\tilde{X}\ ^2B_1$ and 5668 cm^{-1} for the $\tilde{A}\ ^2A_1$ state of H_2S^+ according to Ng and colleagues.[21] The dissociation threshold of 23 700 cm^{-1} for the H_2+S^+ channel is thus ~500 cm^{-1} higher than the barrier to linearity, and all the transitions observed in the PHOFEX spectrum belong to states above the barrier to linearity. Accordingly, in the dipole-allowed $\tilde{A}\ ^2A_1-\tilde{X}\ ^2B_1$ transition of H_2S^+, the highly vibrationally excited $\tilde{X}\ ^2B_1$ states in the bending mode could be strongly observed via the nonadiabatic rovibronic coupling. As noted earlier, since the S^+ yield is monitored in the PHOFEX spectrum, the relative signal intensity is governed not only by the transition oscillator strength but also by the dissociation efficiency. This aspect will be discussed briefly in the next section. The overall spectral assignment based on earlier reports is given in Fig. 3. Vibronic term values deduced from our PHOFEX spectrum are much improved in terms of the accuracy and precision, compared to previously reported term values, as listed in Table I.[20,21] We have adopted the interpretation of the Ng group for the spectral assignment for $\tilde{A}(0,n,0)$ K states where (n_1,n_2,n_3) represents the vibrational quantum numbers for symmetric stretching, bending, or asymmetric stretching modes, respectively. It should be noted here that the K quantum number at the linear geometry is defined as $K=|\pm\Lambda\pm l|$ where Λ and l represent the electronic orbital and vibrational angular momentum quantum numbers,[35] respectively, whereas it corresponds to the K_a quantum number in the bent representation since the a-axis of the bent molecule converges to the HSH bond axis of the linear molecule in the bent-to-quasilinear transition. The $\tilde{A}(0,6,0)$ with K

TABLE II. Rovibronic term values (cm^{-1}) appeared in the MATI-PHOFEX spectra of $H_2S^+(\tilde{A}\ ^2A_1)$ and their vibrational and rotational assignments. Each transition is designated by $^{\Delta Ka}\Delta N_{Ka'',Kc''}$. For each transition ($K \neq 0$), the first and second rows represent the (+)1/2 and (−)1/2 spin-orbit components, respectively. The calculated values (cm^{-1}) are obtained from the ASYMROTWIN program which is used for the reproduction of simulation spectra at the rotational temperature of 30 K while the ortho to para ratio is fixed at 3:1.

		$K(K_a)=0$					
		$v_2''=24$		$v_2'=8$		$v_2'=9$	
Branch	Rotational transition	Obs.[a]	Calc.[b]	Obs.	Calc.	Obs.	Calc.
$^RQ_{0,N}$	$1_{11}-1_{01}$		24 399	⋯	24 932	25 943	25 943
$^RQ_{1,N}$	$2_{20}-2_{12}$	⋯	24 429	⋯	24 977	⋯	25 989
	$3_{21}-3_{13}$	⋯	24 434	24 977	24 976	⋯	25 987
$^PR_{1,N-1}$	$2_{02}-1_{10}$	⋯	24 404	⋯	24 931	⋯	25 943
	$3_{03}-2_{11}$	⋯	24 405	24 932	24 932	25 941	25 941
$^PQ_{1,N}$	$1_{01}-1_{11}$	24 383	24 385	24 914	24 914	25 926	25 926
	$2_{02}-2_{12}$	⋯	24 385	⋯	24 913	⋯	25 924
	$3_{03}-3_{13}$	⋯	24 385	⋯	24 912	⋯	25 921
$^PQ_{2,N-1}$	$2_{11}-2_{21}$	24 375	24 375	24 912	24 912	25 924	25 924
$^PQ_{2,N-2}$	$3_{12}-2_{20}$	24 401	24 401	⋯	24 941	⋯	25 953
$^PP_{1,N-1}$	$0_{00}-1_{10}$	24 371	24 370	⋯	24 900	⋯	25 912
	$1_{01}-2_{11}$		24 351	24 881	24 880	25 892	25 892
	$2_{02}-3_{12}$	24 332	24 331	⋯	24 858	⋯	25 869

		$K(K_a)=1$					
		$v_2'=7$		$v_2'=8$		$v_2''=24$	
Branch	Rotational transition	Obs.	Calc.	Obs.	Calc.	Obs.	Calc.
$^RR_{0,N}$	$1_{10}-0_{00}$	24 341	24 341	25 367	25 367	25 261	25 262
		24 378	24 378	25 407	25 407	25 298	25 298
	$2_{11}-1_{01}$	⋯	24 347	⋯	25 373	⋯	25 268
		⋯	24 390	⋯	25 419	25 304	25 304
	$3_{12}-2_{02}$	24 353	24 353	25 379	25 379	25 275	25 275
		⋯	24 402	⋯	25 432	⋯	25 309
$^RQ_{0,N}$	$1_{11}-1_{01}$	24 328	24 329	25 355	25 355	25 252	25 252
		⋯	24 362	⋯	25 392	⋯	25 283
	$2_{12}-2_{02}$	⋯	24 326	⋯	25 354	⋯	25 257
		⋯	24 356	25 388	25 388	⋯	25 275
	$3_{13}-3_{03}$	⋯	24 325	⋯	25 355	⋯	25 266
		⋯	24 349	⋯	25 384	⋯	25 266
$^RQ_{1,N}$	$2_{20}-2_{12}$	⋯	24 370	25 400	25 400	25 292	25 292
		⋯	24 407	⋯	25 451	⋯	25 323
$^RQ_{1,N-1}$	$2_{21}-2_{11}$	⋯	24 358	⋯	25 389	⋯	25 280
		⋯	24 395	⋯	25 439	⋯	25 311
$^RP_{0,N}$	$1_{10}-2_{02}$	⋯	24 304	⋯	25 330	⋯	25 225
		⋯	24 342	⋯	25 371	⋯	25 261
$^PR_{2,N-1}$	$3_{13}-2_{21}$	⋯	24 340	⋯	25 370	⋯	25 281
		24 364	24 364	⋯	25 399	⋯	25 281
$^PR_{2,N-2}$	$3_{12}-2_{20}$	⋯	24 333	⋯	25 359	⋯	25 255
		⋯	24 382		25 412	⋯	25 289
$^PQ_{1,N}$	$2_{02}-2_{12}$	⋯	24 309	⋯	25 336	⋯	25 237
		⋯	24 345	25 371	25 371	⋯	25 262
$^PQ_{2,N-1}$	$2_{11}-2_{21}$	⋯	24 306	⋯	25 333	⋯	25 228
		24 349	24 349	25 378	25 378	25 263	25 263
	$3_{12}-3_{22}$	⋯	24 296	⋯	25 322	⋯	25 219
			24 346		25 375	⋯	25 252
$^PQ_{2,N-2}$	$2_{12}-2_{20}$	⋯	24 306	⋯	25 334	⋯	25 237
		24 336	24 336	⋯	25 368	⋯	25 255
$^PP_{2,N-1}$	$1_{11}-2_{21}$	24 288	24 288	25 314	25 314	⋯	25 212
		⋯	24 321		25 351	⋯	25 242
	$2_{12}-3_{22}$	⋯	24 269	⋯	25 297	⋯	25 200
		⋯	24 299	⋯	25 331	⋯	25 218

TABLE II. (*Continued.*)

		$K(K_a)=1$					
		$v_2'=7$		$v_2'=8$		$v_2''=24$	
Branch	Rotational transition	Obs.[a]	Calc.[b]	Obs.	Calc.	Obs.	Calc.
$^PP_{2,N-2}$	$1_{10}-2_{20}$	24 285	24 284	⋯	25 310	25 205	25 205
		⋯	24 322	25 350	25 351	25 241	25 241
	$2_{11}-3_{21}$	⋯	24 257	⋯	25 283	⋯	25 178
		⋯	24 299	⋯	25 328	⋯	25 214

		$K(K_a)=2$			
		$v_2'=7$		$v_2'=8$	
Branch	Rotational transition	Obs.	Calc.	Obs.	Calc.
$^RR_{0,N}$	$2_{11}-1_{01}$	⋯	24 557	⋯	25 715
		⋯	24 583	25 746	25 746
	$3_{12}-2_{02}$	24 562[c]	24 562	⋯	25 718
		⋯	24 589	⋯	25 753
$^PR_{2,N-2}$	$3_{12}-2_{20}$	⋯	24 542	⋯	25 698
		24 569	24 569	⋯	25 733
$^RR_{1,N}$	$2_{21}-1_{11}$	24 604	24 604	25 763	25 763
		24 624	24 624	25 792	25 792
	$3_{22}-2_{12}$	24 608[c]	24 608	25 765	25 765
		⋯	24 631	⋯	25 801
$^RR_{1,N-1}$	$2_{20}-1_{10}$	24 600[c]	24 600	25 760	25 760
		⋯	24 620	25 788	25 788
	$3_{21}-2_{11}$	⋯	24 597	⋯	25 753
		24 618[c]	24 618	25 789	25 789
$^RQ_{1,N}$	$2_{20}-2_{12}$	⋯	24 582	⋯	25 741
		⋯	24 601		25 769
	$3_{21}-3_{13}$	⋯	24 577	⋯	25 733
		⋯	24 599	⋯	25 769
$^RQ_{1,N-1}$	$2_{21}-2_{11}$	⋯	24 570	25 729	25 729
		24 589[c]	24 589	25 757	25 757
	$3_{22}-3_{12}$		24 554	25 711	25 711
			24 576	⋯	25 747
$^PQ_{1,N-2}$	$3_{21}-3_{31}$		24 533	⋯	25 690
		⋯	24 555	⋯	25 725
$^PP_{0,N-2}$	$2_{21}-3_{31}$	⋯	24 506	⋯	25 665
		⋯	24 526	⋯	25 694
$^PP_{0,N-3}$	$2_{20}-3_{30}$	⋯	24 504	⋯	25 663
		⋯	24 524	⋯	25 692

[a]The rovibronic term values (cm^{-1}) appeared in the MATI-PHOFEX spectra.
[b]The calculated values (cm^{-1}) obtained from the ASYMROTWIN program.
[c]Term values obtained from PHOFEX spectrum of $\tilde{A}(0,7,0;K=2)$ band.

$=3$ or $\tilde{A}(0,6,0)$ with $K=4$ levels are near the barrier to linearity according to the assignment by the Ng group and the PHOFEX spectrum here starts just above those levels (*vide supra*). Spin-orbit split states have been newly identified in the highly resolved PHOFEX spectrum, giving the precise spin-orbit coupling constants for various vibronic states. The $K=0$ state of $\tilde{X}(0,24,0)$ vibronic band at $\sim 24\,383$ cm^{-1} is newly identified, and its strong signal intensity in the PHOFEX spectrum is quite striking. These features are discussed in the next section. Exact spectroscopic values have been deduced from the asymmetric rigid-rotor simulation based on the appropriate rovibronic spectral assignments given by MATI-PHOFEX spectra as follows.

C. MATI-PHOFEX ($\tilde{A}\,^2A_1 \leftarrow \tilde{X}\,^2B_1$) spectra

The spectral assignment of individual bands even in the highly resolved PHOFEX spectrum of H_2S^+ is certainly a quite formidable task because of the intrinsic spectral complexity brought by strong couplings involved in the bent-to-quasilinear transition especially in the energy region above the barrier to linearity. In this respect, the selection of only a few rotational quantum states in the ground H_2S^+ using the MATI spectroscopic technique is very helpful for the unambiguous spectral assignment. The energy separation of vibronic levels with different K quantum numbers, due to the strong Renner–Teller interaction above the barrier to linearity, is somewhat irregular which cannot be reproduced by the

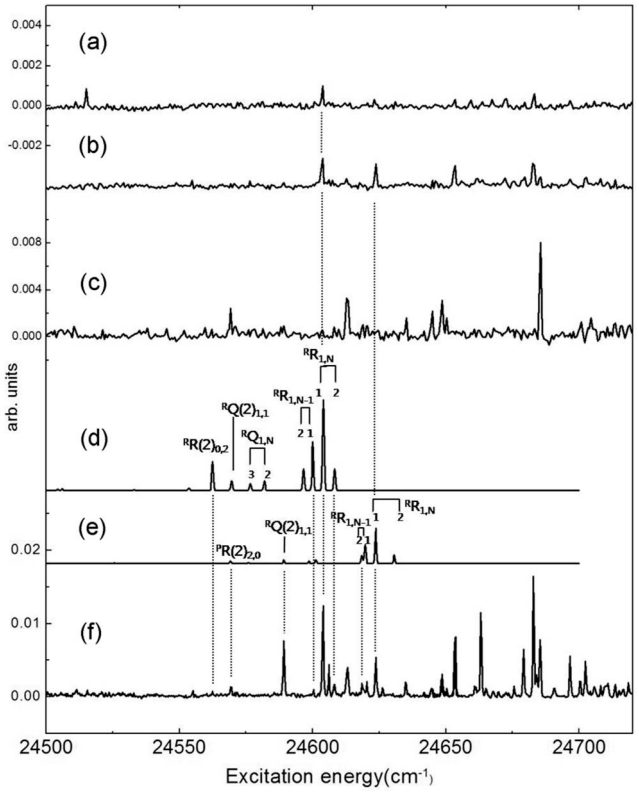

FIG. 5. MATI-PHOFX spectra of $\tilde{A}(0,7,0;K=2)$ taken via (a) RB0, (b) RB1, and (c) RB2 transitions. The simulations for (+)1/2 and (−)1/2 spin-orbit states are shown in (d) and (e), respectively. The PHOFEX spectrum is in (f).

rigid rotor Hamiltonian. Such a large coupling effect had been intensively studied, and the K assignment of each vibronic level according to the full Hamiltonian developed by Duxbury and co-workers[1,3] is quite convincing as shown in Fig. 3 and Table I. Ironically, the large K-dependent coupling effect makes possible the application of the rigid asymmetric rotor Hamiltonian to the analyses of rovibronic transitions which belong to specific vibronic band with the specific K quantum number. Intriguingly, the symmetry selection rule regarding K quantum number has led us to confirm the K assignment. The vibronic origin term values ($T_{v,K,\Sigma=\pm 1/2}$) and relevant spectroscopic parameters regarding the electronically excited state of H_2S^+ are derived through least-squares fits with the ASYMROTWIN program[36] whereas values from Ref. 37 are used for rotational constants of the ground state $\tilde{X}\,^2B_1$. Spin-orbit coupling is taken to be the strongly localized interaction in $H_2S^+(\tilde{A}\,^2A_1)$, and the value of $A^{SO}_{v,K}$ is obtained from the equation of $(T_{v,K,\Sigma=+1/2}-T_{v,K,\Sigma=-1/2})=A^{SO}_{v,K}$, according to Duxbury *et al.*[1] The Gaussian function with a full width at half maximum of 0.7 cm^{-1} is used for the reproduction of the individual transition lines to give the simulation spectra at the rotational temperature of 30 K. Nuclear spin statistics of 3:1 for the ortho to para ratio are strictly considered in the simulation.

In the 24 250–24 400 cm^{-1} region, $K=1$ band of the $\tilde{A}(0,7,0)$ state, $\tilde{A}(0,7,0;K=1)$, is observed, and it is quite obvious that the C-type transition prevails in this dipole-allowed $\tilde{A}\,^2A_1-\tilde{X}\,^2B_1$ transition, Fig. 4. The MATI-PHOFEX spectrum taken by the RB0 excitation shows the remarkable simplification of the spectrum giving two major strongly observed bands at 24 341 and 24 378 cm^{-1} corresponding to the $^RR_{0,0}$ transitions of (+)1/2 and (−)1/2 spin-orbit components, respectively, according to our asymmetric rotor simulation. Here the superscript "R" represents that $\Delta K_a=(K_{a'}-K_{a''})=+1$ whereas the normal R means that $\Delta N=+1$. Similarly, the superscript "Q" or "P" represents that $\Delta K_a=(K_{a'}-K_{a''})=0$ or -1, respectively, whereas the normal Q or P corresponds to the case of $\Delta N=0$ or -1, respectively The subscript values represent $K_{a''}$ and $K_{c''}$ quantum numbers of H_2S^+ in the ground state. Accordingly $^RR_{0,0}$ represents the $1_{10}(\tilde{A}\,^2A_1)-0_{00}(\tilde{X}\,^2B_1)$ transition. The experimental finding that two bands associated with $1_{10}-0_{00}$ transitions of two spin-orbit states are strongly observed in the MATI-PHOFEX spectrum via RB0 confirms the $K=1$ assignment of the $\tilde{A}(0,7,0)$ level. In the MATI-PHOFEX taken via the RB1 transition, the $^RQ_{0,1}$ branch associated with the $1_{11}(\tilde{A}\,^2A_1)-1_{01}(\tilde{X}\,^2B_1)$ transition is strongly observed, as expected. The ground H_2S^+ is mainly populated in the 1_{01} and 2_{02} states in the MATI-PHOFEX spectrum via RB1′. Therefore, $^RQ_{0,1}$ and $^RQ_{0,2}$ branches of $1_{11}(\tilde{A}\,^2A_1)-1_{01}(\tilde{X}\,^2B_1)$ and $3_{12}(\tilde{A}\,^2A_1)-2_{02}(\tilde{X}\,^2B_1)$ transitions, respectively, are found to be significantly enhanced. In the MATI-PHOFEX spectrum via RB2, 2_{11}, 2_{20}, and 2_{21} states of the ground H_2S^+ are mainly populated in the $\tilde{X}\,^2B_1$ state, giving the signal enhancement for $^PP_{2,0}$ and $^PP_{2,1}$ bands of the (+)1/2 spin-orbit state corresponding to $1_{10}(\tilde{A}\,^2A_1)-2_{20}(\tilde{X}\,^2B_1)$ and $1_{11}(\tilde{A}\,^2A_1)-2_{21}(\tilde{X}\,^2B_1)$ transitions, respectively. The $^PQ_{2,0}$ and $^PQ_{2,1}$ transitions associated with the $2_{10}(\tilde{A}\,^2A_1)-2_{20}(\tilde{X}\,^2B_1)$ and $2_{11}(\tilde{A}\,^2A_1)-2_{21}(\tilde{X}\,^2B_1)$ transitions of the (−)1/2 spin-orbit state, respectively, are also enhanced in the same spectrum.

The most striking feature of the PHOFEX spectrum in the 24 250–24 400 cm^{-1} region shown in Fig. 4(h) is the experimental observation of the two most strongly observed peaks at 24 371 and 24 383 cm^{-1} which do not belong to the $\tilde{A}\,^2A_1-\tilde{X}\,^2B_1$ transition. The band at 24 383 cm^{-1} is strongly enhanced also in all MATI-PHOFEX spectra as shown in Figs. 4(a)–4(d), indicating that the upper state in this particular transition may be strongly perturbed through the severe rovibronic coupling. From the assignment of the $\tilde{X}(0,23,0;K=0)$ band at ~23 622 cm^{-1} given by the Ng group, we tentatively assign these bands as the transitions to the $\tilde{X}(0,24,0;K=0)$ state since the additional energy of ~762 cm^{-1} may correspond to one quantum of the bending vibration in the ground state. The $^PP_{1,0}$ and $^PQ_{1,1}$ bands associated with the $0_{00}-1_{10}$ and $1_{01}-1_{11}$ transitions may be responsible for these strong peaks observed at 24 371 and 24 383 cm^{-1}, respectively. The intensity borrowing through nonadiabatic rovibronic coupling between optically bright $\tilde{A}(0,7,0;K=1)$ and dark $\tilde{X}(0,24,0;K=0)$ states should be responsible for the appearance of these bands, though the detailed rotational state assignment is not straightforward at the present time. The abnormally strong intensities of the PHOFEX signals associated with these $\tilde{X}(0,24,0;K=0)$

TABLE III. Spectroscopic parameter values (cm^{-1}) of the upper state from the simulation.

Rotational constants	$\tilde{X}(0,0,0)$	$\tilde{A}(0,7,0)$				$\tilde{X}(0,24,0)$		
		$K=1$		$K=2$		$K=0$	$K=1$	
Σ [a]		(+)1/2	(−)1/2	(+)1/2	(−)1/2		(+)1/2	(−)1/2
Origin		24 316	24 351	24 525	24 552	24 389	25 238	25 273
A	10.17	20.21	20.65	21.30	19.24	16.24	19.99	19.61
B	8.59	4.63	6.97	5.17	5.12	4.08	4.03	5.25
C	4.57	5.36	3.44	3.68	4.64	7.41	7.91	3.44
A_{av} [b]		20.43		20.27		16.24	19.80	
$\bar{B}$ [c]		5.00	5.21	4.43	4.88	5.75	5.97	4.35
$\bar{B}_{av}$ [d]		5.11		4.66			5.16	
q [e]		−0.37	1.77	0.75	0.24	−1.67	−1.94	0.91
q_{av} [f]		0.70		0.50			−0.52	
$A_{v,K}^{SO}$		−35		−27			−35	

Rotational constants	$\tilde{X}(0,0,0)$	$\tilde{A}(0,8,0)$				$\tilde{A}(0,9,0)$	
		$K=0$	$K=1$		$K=2$		$K=0$
Σ			(+)1/2	(−)1/2	(+)1/2	(−)1/2	
Origin		24 919	25 341	25 375	25 685	25 713	25 931
A	10.17	21.26	21.62	25.40	21.27	20.83	21.26
B	8.59	5.22	4.54	6.76	4.74	4.98	5.47
C	4.57	5.17	5.85	4.25	3.41	5.65	4.51
A_{av}		21.26	23.51		21.05		21.26
$\bar{B}$		5.20	5.20	5.51	4.08	5.32	4.99
$\bar{B}_{av}$			5.36		4.70		
q		0.03	−0.66	1.23	0.67	−0.34	0.48
q_{av}			0.29		0.17		
$A_{v,K}^{SO}$			−34		−28		

[a]Spin quantum number.
[b]Average of A rotational constants in two spin-orbit states.
[c]Average of rotational constants B and C, $\bar{B}=(B+C)/2$.
[d]Average of $\bar{B}$'s in two spin-orbit states.
[e]The difference of rotational constants B and C, $q=(B-C)/2$.
[f]Average of two values of q in two spin-orbit states.

bands may also indicate that the reaction efficiency for the H_2+S^+ dissociation channel is greatly enhanced when the highly vibrationally excited state of the ground H_2S^+ is directly prepared. This finding is consistent with the reaction mechanism in which the ground state of H_2S^+, as mentioned above, couples to the repulsive quartet state leading to the formation of H_2+S^+ products.[28–30] Experiment and simulation are compared for individual transitions in Table II, providing accurate and precise energies for properly identified rotational transitions. Term values of the $\tilde{A}(0,7,0;K=1)$ band, rotational constants, and spin-orbit coupling constants are deduced from the comparison of the experiment with the asymmetric rotor simulation based on the assignment based on MATI-PHOFEX spectra via various sets of initial rotational states.

The similar strategy has been applied to the spectral assignment of the $\tilde{A}(0,7,0;K=2)$ band, Fig. 5. In this case, since the upper K ($K_{a'}$) value is equal to 2, the MATI-PHOFEX signal via RB1 is found to be mostly active, giving the strong $^RR_{1,1}$ band corresponding to the $2_{21}(\tilde{A}\,^2A_1)-1_{11}(\tilde{X}\,^2B_1)$ transition for both spin-orbit states. In the MATI-PHOFEX spectrum via RB0, except a small peak of the $^RR_{1,1}$ branch probably due to the $1_{11}(\tilde{X}\,^2B_1)$ contribution in the RB0 excitation, no other bands stand out because of the C-type selection rule of $\Delta K_a=\pm 1$. The $2_{21}(\tilde{A}\,^2A_1)-2_{11}(\tilde{X}\,^2B_1)$ transition ($^RQ_{1,1}$) is identified in the MATI-PHOFEX spectrum taken via RB2. Not all bands in the MATI-PHOFEX spectra are assignable with our simulation, suggesting that the rovibronic coupling in this spectral region of $K=2$ should be much more complex. It is interesting to note that the averaged A rotational constant of the $\tilde{A}(0,7,0;K=1)$ band is slightly larger than that of the $\tilde{A}(0,7,0;K=2)$ band. This may indicate that the H_2S^+ in the $K=1$ band tends to follow the linear type rotational motion compared to the case of $K=2$, giving the relatively higher spin-orbit coupling energy for $K=1$, Table III.

For $\tilde{A}(0,8,0;K=0)$ band, as expected, no spin-orbit

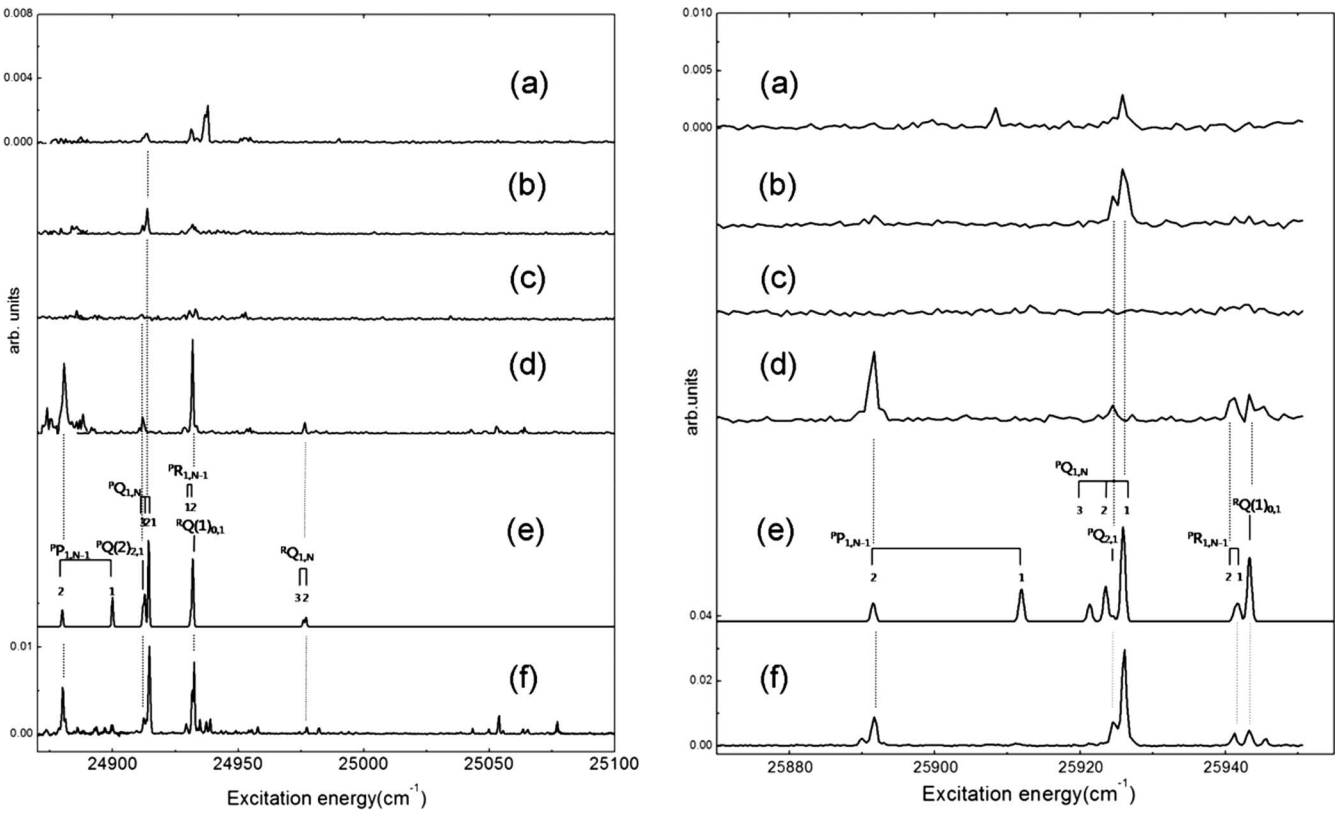

FIG. 6. Left: MATI-PHOFEX spectra taken via (a) RB0, (b) RB1, (c) RB1′, and (d) RB2 transitions, respectively. The simulation for $\tilde{A}(0,8,0;K=0)$ is shown in (e) with the PHOFEX spectrum in (f). Right: For $\tilde{A}(0,9,0;K=0)$ level, MATI-PHOFEX spectra via (a) RB0, (b) RB1, (c) RB1′, and (d) RB2 are shown with the (e) simulation and (f) PHOFEX spectrum

splitting is observed in the spectrum. The PHOFEX spectrum is very well reproduced by the simulation, Fig. 6. MATI-PHOFEX spectra taken via RB0, RB1, RB1′, and RB2 identify rotational transitions in a proper way. Namely, the $^{P}Q_{1,1}$ band due to the $1_{01}(\tilde{A}\,^{2}A_1)-1_{11}(\tilde{X}\,^{2}B_1)$ transition is strongly observed in the MATI-PHOFEX spectrum via RB1 whereas the $^{P}P_{1,1}$ and $^{P}R_{1,1}$ bands due to the $1_{01}(\tilde{A}\,^{2}A_1)-2_{11}(\tilde{X}\,^{2}B_1)$ and $3_{03}(\tilde{A}\,^{2}A_1)-2_{11}(\tilde{X}\,^{2}B_1)$ transitions, respectively, are obviously enhanced in the MATI-PHOFEX spectrum taken via RB2. It should be noted here that the transition with $\Delta K_c=2$ has also been observed. The $\tilde{A}(0,9,0;K=0)$ band in the PHOFEX spectrum observed in the 25 880–25 950 cm^{-1} region is also quite well reproduced by the asymmetric rotor simulation, Fig. 6. The MATI-PHOFEX spectrum via RB1 shows the enhancement in the $^{P}Q_{1,1}$ band due to the $1_{01}(\tilde{A}\,^{2}A_1)-1_{11}(\tilde{X}\,^{2}B_1)$ transition whereas the $^{P}P_{1,1}$ band of the $1_{01}(\tilde{A}\,^{2}A_1)-2_{11}(\tilde{X}\,^{2}B_1)$ transition is strongly observed in the MATI-PHOFEX spectrum taken via RB2. This is consistent with the expectation that the upper state with $K=0$ is less perturbed.

The $K=2$ band of $\tilde{A}(0,8,0)$ level is well explainable with the asymmetric rotor simulation for two spin-orbit states, Fig. 7. MATI-PHOFEX spectra are extremely helpful for the identification of specific rotational transitions. For instance, in the MATI-PHOFEX spectrum via RB1, the $^{R}R_{1,1}$ band due to the $2_{21}(\tilde{A}\,^{2}A_1)-1_{11}(\tilde{X}\,^{2}B_1)$ transition is strongly observed for both spin-orbit states whereas the $^{R}R_{1,0}$ band corresponding to the $2_{20}(\tilde{A}\,^{2}A_1)-1_{10}(\tilde{X}\,^{2}B_1)$ is enhanced in the MATI-PHOFEX spectrum via RB1′. Similarly to the case of the $\tilde{A}(0,7,0;K=2)$ band (*vide supra*), in the MATI-PHOFEX spectrum via RB0, no other bands except a small peak of the $^{R}R_{1,1}$ branch are significantly observed because of the selection rule of $\Delta K_a=\pm 1$. The $^{R}Q_{1,1}$ and $^{R}R_{1,2}$ branches associated with the $2_{21}(\tilde{A}\,^{2}A_1)-2_{11}(\tilde{X}\,^{2}B_1)$ and $3_{22}(\tilde{A}\,^{2}A_1)-2_{12}(\tilde{X}\,^{2}B_1)$ transitions, respectively, are greatly enhanced in the MATI-PHOFEX taken via RB2. The experimental observation that only R branches in K are strongly observed in the MATI-PHOFEX spectra in Fig. 7 confirms that those bands in the 25 700–25 800 cm^{-1} region belong to the $K=2$ level.

The $\tilde{A}(0,8,0;K=1)$ band is observed in the 25 300–25 450 cm^{-1} region whereas the newly found $\tilde{X}(0,24,0;K=1)$ band is also weakly observed in the energy range of 25 200–25 320 cm^{-1}, Fig. 8. Four $^{R}R_{0,0}$ bands are strongly observed in the MATI-PHOFEX spectrum taken via RB0 for two spin-orbit states of both $\tilde{A}(0,8,0;K=1)$ and $\tilde{X}(0,24,0;K=1)$ bands. The rotational assignments based on these four rovibronic bands provide quite satisfactory assignments consistent with the simulation, giving the accurate and precise spectroscopic constants involved in the bent-to-quasilinear transition above the barrier to linearity. Interestingly, the A_{av} value of the $\tilde{A}(0,8,0;K=1)$ is also found to be slightly larger than that of the $\tilde{A}(0,8,0;K=2)$ band similarly

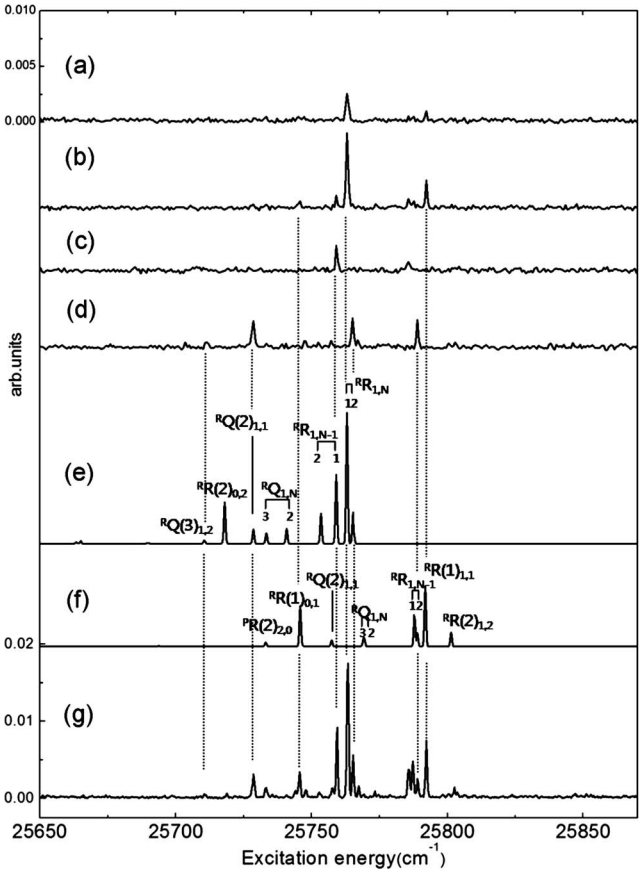

FIG. 7. MATI-PHOFEX spectra taken via (a) RB0, (b) RB1, (c) RB1′, and (d) RB2 transitions to the $\tilde{A}(0,8,0;K=2)$ level. Simulations for (+)1/2 and (−)1/2 spin-orbit components are shown in (e) and (f), respectively. The PHOFEX spectrum is in (g).

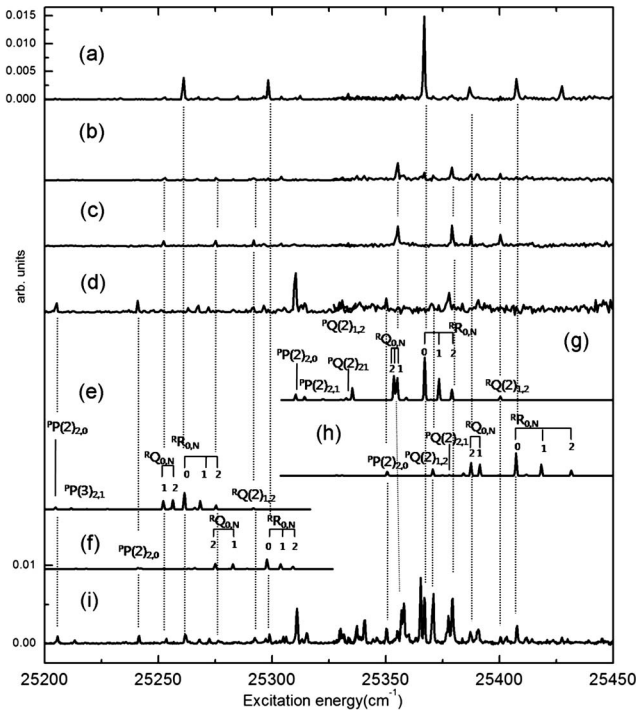

FIG. 8. MATI-PHOFX spectra via (a) RB0, (b) RB1, (c) RB1′, and (d) RB2 transitions in the $\tilde{X}(0,24,0;K=1)$ and $\tilde{A}(0,8,0;K=1)$ bands region. The simulations for $\tilde{X}(0,24,0;K=1)$ are presented for (e) (+)1/2 and (f) (−)1/2 spin-orbit states, whereas those for $\tilde{A}(0,8,0;K=1)$ are shown in (g) and (h) for (+)1/2 and (−)1/2 spin-orbit states, respectively. The PHOFEX spectrum over the 25 200–25 450 cm^{-1} energy region is shown in (i).

to the case of $\tilde{A}(0,7,0)$ band. The spin-orbit coupling constant of −34 cm^{-1} estimated in the $\tilde{A}(0,8,0;K=1)$ band is significantly larger than the value of −28 cm^{-1} for the $\tilde{A}(0,8,0;K=2)$ band whereas the spin-orbit split energy of −35 cm^{-1} for the $\tilde{X}(0,24,0;K=1)$ band is very similar to the value of the $\tilde{A}(0,8,0;K=1)$ band, suggesting that the orientation of the angular momentum with respect to the a principal axis may be critical in the spin-orbit coupling especially above the barrier to linearity. It is interesting to note that in the process of fitting the experimental results for the $\tilde{X}(0,24,0;K=0)$ and $\tilde{X}(0,24,0;K=1)$ bands, the difference between B and C rotational constants, (B-C), becomes largely negative whereas it is positive for the nearby $\tilde{A}(0,7,0;K=1)$ and $\tilde{A}(0,8,0;K=1)$ bands. The fact that the negative value of (B-C) is obtained in the C-type simulation suggests that the actual rotational transitions to $\tilde{X}(0,24,0)$ band belong to the *B*-type transition. This is another evidence of the strong nonadiabatic coupling among $\tilde{A}$ and $\tilde{X}$ states of H_2S^+ as the transition of the dipole-forbidden $\tilde{X}$-$\tilde{X}$ becomes rovibronically allowed by the nonadiabatic coupling.

Before concluding this section, it may be quite meaningful to describe the following experiment which was performed to investigate the nature of the broad bands observed in the MATI spectrum in Fig. 2. In Figs. 2(c)–2(f), the VUV ionization laser wavelength was scanned whereas the photodissociation laser frequency was fixed at the specific $\tilde{A}$-$\tilde{X}$ rovibronic transitions of $1_{10}(\tilde{A}\,^2A_1)-0_{00}(\tilde{X}\,^2B_1)$ of $\tilde{A}(0,7,0;K=1)^-$, $2_{21}(\tilde{A}\,^2A_1)-1_{11}(\tilde{X}\,^2B_1)$ of $\tilde{A}(0,8,0;K=2)^+$, $1_{11}(\tilde{A}\,^2A_1)-1_{01}(\tilde{X}\,^2B_1)$ of $\tilde{A}(0,7,0;K=1)^+$ and $3_{03}(\tilde{A}\,^2A_1)-2_{11}(\tilde{X}\,^2B_1)$ of $\tilde{A}(0,8,0;K=0)$, respectively. These spectra represent the energy distribution of the corresponding rotational states in the ground H_2S^+ and verify our spectral assignments for the MATI spectrum as the main peak positions match the rotational levels obtained by the simulation. Broad spectral features with somewhat long tails at the low-energy region suggest that long-lived Rydberg manifolds converging to closely-spaced rotational levels contribute to the MATI spectrum, as mentioned earlier.

Overall, the PHOFEX spectrum represents the $\tilde{A}\,^2A_1-\tilde{X}\,^2B_1$ excitation spectroscopy of the rotationally cold H_2S^+ above the barrier to linearity. The distinct energy separation between vibronic levels of different *K* quantum numbers makes possible not only the appropriate spectral assignment but also the simulation of individual rotational transitions by adjusting rotational constants of the upper electronic state within each *K* band. It is found out that $\tilde{X}(0,n,0)$ bands, via coupling to the optically active $\tilde{A}$ band, are activated in the PHOFEX spectrum. Especially, the $\tilde{X}(0,24,0;K=0)$ band shows the very strong intensity in the PHOFEX spectrum, suggesting that the direct access of the highly vibrationally

excited state of $\tilde{X}\,^2B_1$ may lead to the efficient dissociation. MATI-PHOFEX spectra taken by the initial selection of only a few rotational states of $H_2S^+(\tilde{X}\,^2B_1)$ are extremely helpful in appropriate assignments of rotational transitions. The experiment is well reproduced by the simulation. Accordingly, spectroscopic constants such as term values, rotational constants for each spin-orbit split vibronic level are quite precisely estimated and listed in Table III. The spin-orbit splitting constant is strongly dependent on the character of the vibronic level, and it changes the sign near the barrier to linearity. Negative spin-orbit constants determined for $\tilde{A}(0,7,0)$ and $\tilde{A}(0,8,0)$ bands are consistent with the trend which had previously been predicted by Duxbury *et al.*[1] It is amazing that the rigid asymmetric rotor Hamiltonian works fairly well at least in the narrow energy range for a specific vibronic level with a specific K number.

IV. CONCLUSION

Above the barrier to linearity in the bent-to-quasilinear transition of the triatomic molecule, the spectroscopic feature is generally quite complex due to strong Renner–Teller and spin-orbit interactions. Our combined use of MATI and PHOFEX techniques provides the very useful mean to disentangle the complicated spectral structures associated with the bent-to-quasi-linear rovibronic transitions of H_2S^+. By narrowing down the population of the rotational states of $H_2S^+(\tilde{X}\,^2B_1)$, the great simplification has been achieved, allowing for unambiguous assignments of individual rotational transition bands. The relative spectral intensity in the PHOFEX spectrum reflects also the quantum state specific photodissociation cross section which would need the further investigation.

ACKNOWLEDGMENTS

This work was supported by the National Research Foundation of Korea (Grant Nos. 2009-0063163, 2009-0053131, 2009-0082847, and C00401)

[1] G. Duxbury, C. Jungen, and J. Rostas, Mol. Phys. **48**, 719 (1983).
[2] G. Duxbury, M. Horani, and J. Rostas, Proc. R. Soc. London, Ser. A **331**, 109 (1972).
[3] R. N. Dixon, G. Duxbury, M. Horani, and J. Rostas, Mol. Phys. **22**, 977 (1971).
[4] C. Jungen and A. J. Merer, Mol. Phys. **40**, 1 (1980).
[5] C. Jungen, K. E. J. Hallin, and A. J. Merer, Mol. Phys. **40**, 65 (1980).
[6] C. Jungen, K. E. J. Hallin, and A. J. Merer, Mol. Phys. **40**, 25 (1980).
[7] R. N. Dixon, Trans. Faraday Soc. **60**, 1363 (1964).
[8] T. Barrow, R. N. Dixon, and G. Duxbury, Mol. Phys. **27**, 1217 (1974).
[9] C. Jungen and A. J. Merer, *Molecular Spectroscopy, Modern Research*, ed. K. N. Rao and C. W. Mathews, Academic Press, New York and London, 1976).
[10] A. W. Potts and W. C. Price, Proc. R. Soc. London, Ser. A **326**, 181 (1972).
[11] J. Delwiche and P. Natalis, Chem. Phys. Lett. **5**, 564 (1970).
[12] S. Durmaz, G. H. King, and R. J. Suffolk, Chem. Phys. Lett. **13**, 304 (1972).
[13] D. C. Frost, A. Katrib, C. A. McDowell, and R. A. N. McLean, Int. J. Mass Spectrom. Ion Phys. **7**, 485 (1971).
[14] W. Domcke, L. S. Cederbaum, J. Schirmer, W. von Niessen, and J. P. Maier, J. Electron Spectrosc. Relat. Phenom. **14**, 59 (1978).
[15] R. T. Wiedmann, M. G. White, K. Wang, and V. McKoy, J. Chem. Phys. **100**, 4738 (1994).
[16] H. F. Prest, W. B. Tzeng, J. M. Brom, Jr., and C. Y. Ng, Int. J. Mass Spectrom. Ion Phys. **50**, 315 (1983).
[17] M. Y. Adam, P. Morin, C. Cauletti, and M. N. Piancastelli, J. Electron Spectrosc. Relat. Phenom. **36**, 377 (1985).
[18] C. E. Brion, Y. Iida, and J. P. Thomson, Chem. Phys. **101**, 449 (1986).
[19] L. Karlsson, L. Mattsson, R. Jadrny, T. Bergmark, and K. Siegbahn, Phys. Scr. **13**, 229 (1976).
[20] P. Baltzer, L. Karlsson, M. Lundqvist, B. Wannberg, D. M. P. Holland, and M. A. MacDonald, Chem. Phys. **195**, 403 (1995).
[21] M. Hochlaf, K. M. Weitzel, and C. Y. Ng, J. Chem. Phys. **120**, 6944 (2004).
[22] S. Choi, K.-W. Choi, S. K. Kim, S. Chung, and S. Lee, J. Phys. Chem. A **110**, 13183 (2006).
[23] K.-W. Choi, S. Choi, S. J. Baek, and S. K. Kim, J. Chem. Phys. **126**, 034308 (2007).
[24] M. Lee and M. S. Kim, J. Chem. Phys. **126**, 154317 (2007).
[25] Y. J. Bae and M. S. Kim, J. Chem. Phys. **128**, 124324 (2008).
[26] R. T. Wiedmann and M. G. White, Proc. SPIE **1638**, 273 (1992).
[27] J. H. D. Eland, Int. J. Mass Spectrom. Ion Phys. **31**, 161 (1979).
[28] A. D. Webb, N. Kawanaka, R. N. Dixon, and M. N. R. Ashfold, J. Chem. Phys. **127**, 224308 (2007).
[29] A. D. Webb, R. N. Dixon, and M. N. R. Ashfold, J. Chem. Phys. **127**, 224307 (2007).
[30] D. M. Hirst, J. Chem. Phys. **118**, 9175 (2003).
[31] G. Hirsch and P. J. Bruna, Int. J. Mass Spectrom. Ion Phys. **36**, 37 (1980).
[32] C. P. Edwards, C. S. Maclean, and P. J. Sarre, Chem. Phys. Lett. **87**, 11 (1982).
[33] V. H. Dibeler and H. M. Rosenstock, J. Chem. Phys. **39**, 3106 (1963).
[34] G. R. Möhlmann and F. J. de Heer, Chem. Phys. Lett. **36**, 353 (1975).
[35] G. Herzberg, *Molecular Spectra and Molecular Structure Vol. 3: Electronic Spectra and Electronic Structure of Polyatomic Molecules* (Van Nostrand Reinhold, New York, 1966).
[36] R. H. Judge and D. J. Clouthier, Comput. Phys. Commun. **135**, 293 (2001).
[37] S. Lahmar, Z. Ben Lakhdar, G. Chambaud, and P. Rosmus, J. Mol. Struct.: THEOCHEM **333**, 29 (1995).